Article

Ti^{3+} Defective SnS$_2$/TiO$_2$ Heterojunction Photocatalyst for Visible-Light Driven Reduction of CO$_2$ to CO with High Selectivity

Aiguo Han [1], Mei Li [1], Shengbo Zhang [1], Xinli Zhu [1], Jinyu Han [1], Qingfeng Ge [1,2] and Hua Wang [1,*]

[1] Key Laboratory for Green Chemical Technology of Ministry of Education, Collaborative Innovation Center of Chemical Science and Engineering, School of Chemical Engineering and Technology, Tianjin University, Tianjin 300072, China; hanaiguo@tju.edu.cn (A.H.); li1528619076@163.com (M.L.); zhang4580922@163.com (S.Z.); xinlizhu@tju.edu.cn (X.Z.); hanjinyu@tju.edu.cn (J.H.); qge@chem.siu.edu (Q.G.)

[2] Department of Chemistry and Biochemistry, Southern Illinois University, Carbondale, IL 62901, USA

* Correspondence: tjuwanghua@tju.edu.cn; Tel.: +86-1392-069-3419

check for updates

Abstract: In recent years, defective TiO$_2$-based composite nanomaterials have received much attention in the field of photocatalysis. In this work, TiB$_2$ was used as a precursor to successfully prepare Ti^{3+} defective TiO$_2$ (TiO$_2$-B) with a truncated bipyramidal structure by a one-step method. Then, the SnS$_2$ nanosheets were assembled onto the as-prepared TiO$_2$-B through simple hydrothermal reaction. TiO$_2$-B exhibits strong visible light absorption properties, but the recombination rate of the photo-generated electron-hole pair was high and does not exhibit ideal photocatalytic performance. Upon introducing SnS$_2$, the heterojunction catalyst SnS$_2$-Ti^{3+} defective TiO$_2$ (SnS$_2$/TiO$_2$-B) not only possesses the strong light absorption from UV to visible light region, the lowest photo-generated charge recombination rate but also achieves a more negative conduction band potential than the reduction potential of CO$_2$ to CO, and thereby, exhibits the significantly enhanced selectivity and yield of CO in photocatalytic CO$_2$ reduction. Notably, SnS$_2$/TiO$_2$-B produces CO at a rate of 58 μmol$\cdot$h$^{-1}\cdot$g^{-1} with CO selectivity of 96.3% under visible light irradiation, which is 2 and 19 times greater than those of alone TiO$_2$-B and SnS$_2$, respectively. Finally, a plausible photocatalytic mechanism on SnS$_2$/TiO$_2$-B was proposed that the electron transfer between TiO$_2$ and SnS$_2$ follows the Z-scheme mode. Our results present an effective way to gain highly efficient TiO$_2$ based photocatalysts for CO$_2$ reduction by combining different modification methods of TiO$_2$ and make full use of the synergistic effects.

Keywords: photocatalytic CO$_2$ reduction; TiO$_2$ nanoplates; SnS$_2$ nanosheets; Ti^{3+} defective TiO$_2$

1. Introduction

In modern society, the energy crisis and global warming have been two serious issues for human beings to face. As it is known, most of the energy demands are fulfilled through the combustion of fossil fuels, and then the excessive utilization of fossil fuels cause the ever-increasing emission of greenhouse gas CO$_2$, a major contributor to global warming [1,2]. As one of the sustainable "green" approaches towards solving above issues, photocatalytic reduction of CO$_2$ into high value-added chemicals has remarkable advantages in terms of utilizing renewable energy and reducing CO$_2$ emissions simultaneously [3].

Titanium dioxide (TiO$_2$), as a typical semiconductor, has gained lots of interest due to its environmental friendliness, low cost, resistance to light corrosion, and high stability [4–6]. However, it has drawbacks in terms of the ineffective utilization of visible light and low quantum efficiency

due to its wide band gap (3.2 eV) and high recombination of photo-generated electron-hole pairs [7]. Therefore, various strategies have been explored to boost the efficiency of TiO_2 for photocatalytic CO_2 reduction, including controlling TiO_2 crystals facets [8], introducing oxygen vacancies and Ti^{3+} defects [9] and building heterostructures with other semiconductors [10]. From the previous studies, it has been found that single modification route can only improve a specific property of TiO_2, which is far from the requirements of a photocatalyst for achieving the efficient and selective reduction of CO_2. Therefore, it could be an effective way to fabricate highly efficient TiO_2 based photocatalysts by combining different modification methods to make full use of the synergistic effects.

As for the advantage of the faceted TiO_2, it is generally accepted that different TiO_2 facets have quite different surface adsorption properties and surface electronic structures, which determine the adsorption of CO_2 and H_2O, the light absorption and redox potentials of the excited charges, in turn affecting the photocatalytic activity. It has been reported that the photocatalytic activities for CO_2 reduction on different anatase TiO_2 facets are in the order of {010} > {101} > {001} facets [8,11]. In addition, the faceted TiO_2 with co-exposed facets of {101} and {001} could favor the separation and transfer of the photo-generated charge carriers due to the heterojunction between different facets [12]. However, the photocatalytic activities of the faceted TiO_2 are still too low, especially under visible light irradiation. As thus, most studies focus on the further modifications of the faceted TiO_2 to enhance the visible light absorption and promote photo-generated charge separation. One useful way is the introduction of oxygen vacancies and the corresponding Ti^{3+} ions into TiO_2 [13–15]. As reported, the remarkably enhanced and selective photoreduction of CO_2 could be obtained on an oxygen-deficient TiO_2 with co-exposed {101} and {001} facets [16]. Moreover, except the ability to improve visible light absorption, oxygen vacancies could enhance the chemisorption of CO_2 and further mediate the electron transfer to the adsorbed CO_2 to form the key mediate CO_2, which is the initial and crucial step in CO_2 reduction, but unfavorable on the perfect TiO_2 surfaces [17]. Another way to modify the faceted TiO_2 is to construct a TiO_2-semiconductor heterojunction, especially with a semiconductor with strong visible light absorption, which could act as a photosensitizer to promote visible-light-driven photocatalytic CO_2 reduction [18,19]. Based on the individual role of each modification method, it could be expected that a TiO_2-based photocatalyst with features of co-exposed {101} and {001} facets, oxygen vacancies and a heterojunction with a narrow band gap semiconductor, demonstrates a significantly high activity and selectivity towards visible-light-driven photocatalytic CO_2 reduction.

Regarding the preparation of defective TiO_2 materials, post-processes are usually applied through hydrogen thermal treatment or chemical reduction with $NaHB_4$ [20,21]. Recently, a facile one-step method was reported to synthesize defective anatase TiO_2 with co-exposed {101} and {001} facets using TiB_2 as a precursor, which exhibited the strong visible light absorption due to its large amount of Ti^{3+} defects [22,23]. Besides, in respect of the combination of a semiconductor, two-dimensional tin disulfide (SnS_2) nanosheets are a good candidate because of its narrow band gap, easy synthesis, and easy formation of heterojunctions with other materials [24–26]. Zhang et al. reported that a hierarchical nanostructured SnS_2/TiO_2 photocatalyst exhibited excellent visible-light photocatalytic activity in degradation of organic dyes due to the photo-synergistic effects [27].

In our present work, we report a facile approach to synthesize a heterojunction catalyst combing the Ti^{3+} defective TiO_2 nanoplates and SnS_2 nanosheets for enhancing the photocatalytic activity and selectivity towards CO_2 reduction. Firstly, TiB_2 was used as a precursor to successfully prepare Ti^{3+} defective TiO_2 with a truncated bi-pyramidal structure by a one-step method. Then, the SnS_2 nanosheets were assembled onto the as-prepared TiO_2 through simple hydrothermal reaction. In the photocatalytic CO_2 reduction under visible light irradiation, the as-prepared heterojunction catalyst SnS_2-Ti^{3+} defective TiO_2 (SnS_2/TiO_2-B) exhibited superior photocatalytic activity and selectivity to CO compared with catalysts Ti^{3+} defective TiO_2 (TiO_2-B), SnS_2, and SnS_2-TiO_2 without Ti^{3+} defects (SnS_2/TiO_2-W). The excellent photocatalytic performance of SnS_2/TiO_2-B is ascribed to its enhanced absorption of visible light, the reduced recombination rate of photo-generated charge carriers and more negative conduction band potential than the reduction potential of CO_2 to CO. Our work

demonstrates that it is effective to gain highly efficient TiO_2 based photocatalysts for CO_2 reduction through combining different modification of faceted TiO_2 and make full use of the synergistic effects.

2. Results and Discussion

2.1. Synthesis and Characterization

The preparation route of SnS_2/TiO_2-B is illustrated in Figure 1. A certain amount of HF aqueous solution is mixed with the sonicated TiB_2 suspension. Then a hydrothermal reaction of the mixture is conducted in a 100 mL Teflon-lined autoclave at 180 °C for 12 h. After the reaction, the dark blue Ti^{3+} defective TiO_2 (TiO_2-B) is obtained. Then TiO_2-B is mixed with an aqueous solution of Poly (sodium 4-styrenesulfonate) (PSS) for 20 min. The treated TiO_2-B is then dispersed in deionized water in a 100 mL Teflon tube. After adding an appropriate amount of $SnCl_4 \cdot 5H_2O$, thioacetamide (TAA) and acetic acid, the hydrothermal reaction is performed at 160 °C for 12 h. Finally, a heterojunction photocatalyst SnS_2/TiO_2-B is obtained.

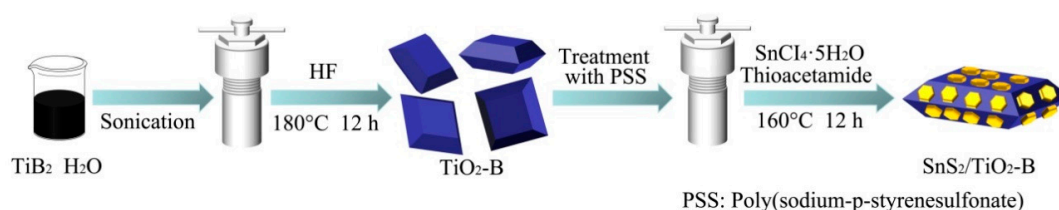**Figure 1.** Schematic illustration for the preparation of SnS_2/TiO_2-B.

The X-ray diffraction (XRD) patterns of SnS_2, TiO_2-B, and SnS_2/TiO_2-B are shown in Figure 2. The XRD peaks of SnS_2 and TiO_2-B are indexed to pure hexagonal phase SnS_2 (berndtite-2H, JCPDS No. 01-089-2358) and tetragonal phase TiO_2 (anatase, JCPDS No. 01-078-2486), respectively [28]. The sample SnS_2/TiO_2-B shows the characteristic peaks of both TiO_2-B and SnS_2, demonstrating that SnS_2 is successfully assembled onto the TiO_2-B. However, the peak intensities corresponding to SnS_2 are very weak, which is ascribed to the low content of SnS_2 in SnS_2/TiO_2-B (7.6 wt.% based on the elemental mapping result) [29]. Besides, the control samples TiO_2-W, SnS_2/TiO_2-W obtained through calcination treatment of TiO_2-B, SnS_2/TiO_2-B in muffle are also characterized and the results are shown in Figure S1. The peaks of TiO_2-W are identical to that of TiO_2-B, indicating that calcination treatment does not change the crystal structure. SnS_2/TiO_2-W also contains peaks of TiO_2-W and SnS_2, indicating the successful combination of SnS_2 and TiO_2-W.
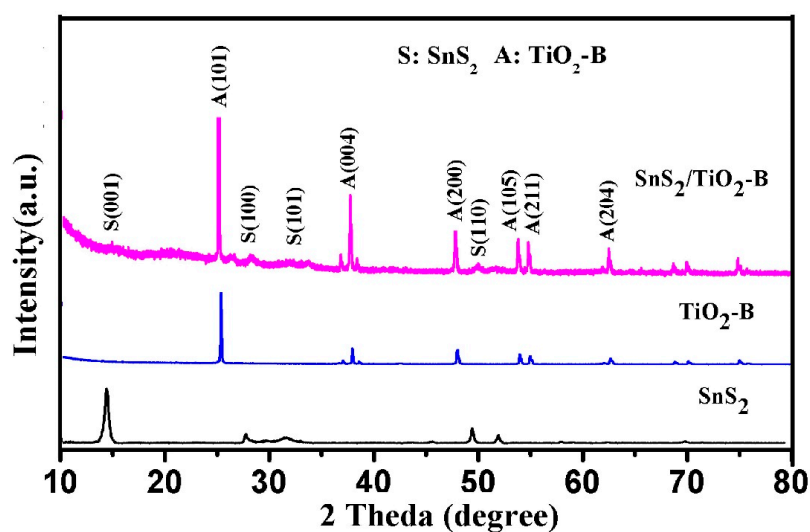
Figure 2. XRD patterns of SnS_2/TiO_2-B, TiO_2-B, and SnS_2.

Figure 3 shows the SEM images of the as-prepared samples TiO_2-B, TiO_2-W, SnS_2/TiO_2-B, and SnS_2/TiO_2-W. From Figure 3a, it can be seen that TiO_2-B presents a nanoplate structure with a size of about 500 to 700 nm wide and a thickness of about 80 nm. In addition, the enlarged SEM image (Figure S2a) of TiO_2-B crystals reveals a truncated bipyramidal structure, in which there are the co-exposed {001} and {101} facets according to the literature [22,30–32]. Figure 3b shows the SEM image of TiO_2-W. It indicates that the nanoplate morphology remains substantially intact after calcination except some flakes forming on the surface. Besides, the optical photographs of TiO_2-B before and after calcination are compared as shown in Figure S2, a significant color change from black blue to white can be observed after calcination in an oxygen atmosphere, meaning that TiO_2-W could hardly absorb visible light due to the absence of Ti^{3+} defects [13]. In addition, it is found that the mass of TiO_2-W increased by about 5 wt.% compared with that of TiO_2-B, indicating the oxidation reaction of the defective TiO_2-B, which could be as evidence that TiO_2-B possesses the oxygen vacancy due to partial reduced state Ti ions. After loading SnS_2 (Figure 3c,d), both SnS_2/TiO_2-B and SnS_2/TiO_2-W present the coating layers consisting of numerous nanosheets with a size of approximately 70 to 100 nm, indicating the successful assembling of SnS_2 on TiO_2-B and TiO_2-W, respectively.

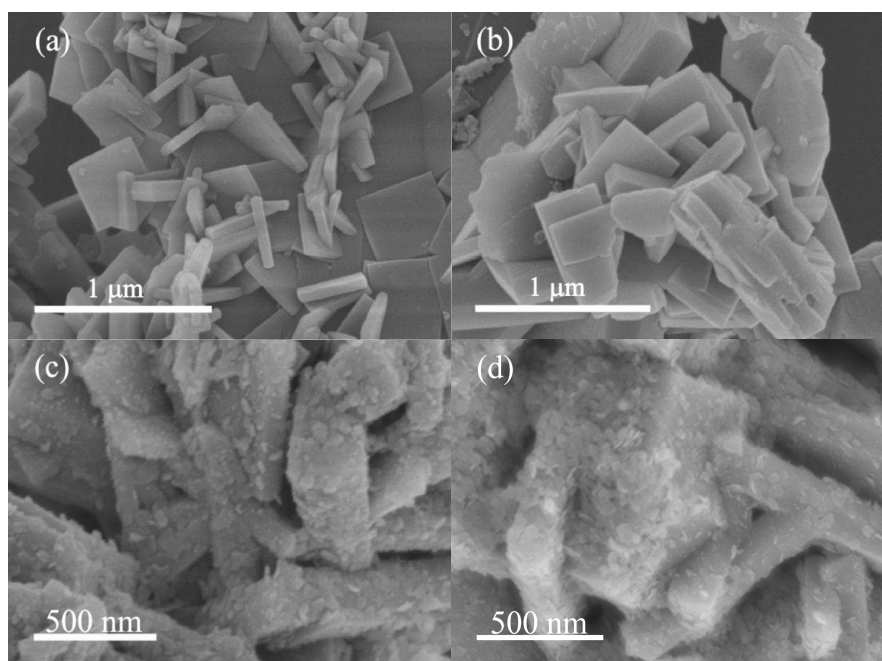**Figure 3.** (**a**) SEM images of TiO_2-B, (**b**) TiO_2-W, (**c**) SnS_2/TiO_2-B, (**d**) SnS_2/TiO_2-W.

Figure 4a shows the typical TEM images of SnS_2/TiO_2-B. From Figure 4a, it can be seen that SnS_2 nanosheets grow flatly or vertically on the TiO_2-B the surface. Furthermore, a high-resolution TEM image of SnS_2 nanosheets (Figure 4b) displays the inter-planar distance of 0.31 nm, which is consistent with that of SnS_2 {100} plane [33]. The selected area electron diffraction (SEAD) pattern (Figure 4c) reveals the presence of both TiO_2 and SnS_2 crystals in the heterostructure SnS_2/TiO_2-B, and a single-crystalline TiO_2-B with co-exposed {101} and {001} facets [12,27,34]. In addition, the magnified HRTEM image (Figure 4d) of the interface region clearly displays the interplanar distances of 0.35 and 0.59 nm, corresponding to the {101} plane of TiO_2 and the {001} plane of SnS_2, respectively. What's more, the TEM elemental mapping of SnS_2/TiO_2-B has been performed to identify the spatial distributions of elements Ti, O, Sn and S, as shown in Figure 4e–i. It is indicated that the elements Sn, S evenly distribute on a support consisting of densely distributed Ti, O elements. The above results clearly demonstrate that the TiO_2-B nanoplate surfaces are coated by SnS_2 and the interface heterojunction forms between TiO_2-B and SnS_2. The tight heterojunction structure of SnS_2/TiO_2-B would benefit the interfacial charge transfer spatially, and thereby increase the photocatalytic activity [35].

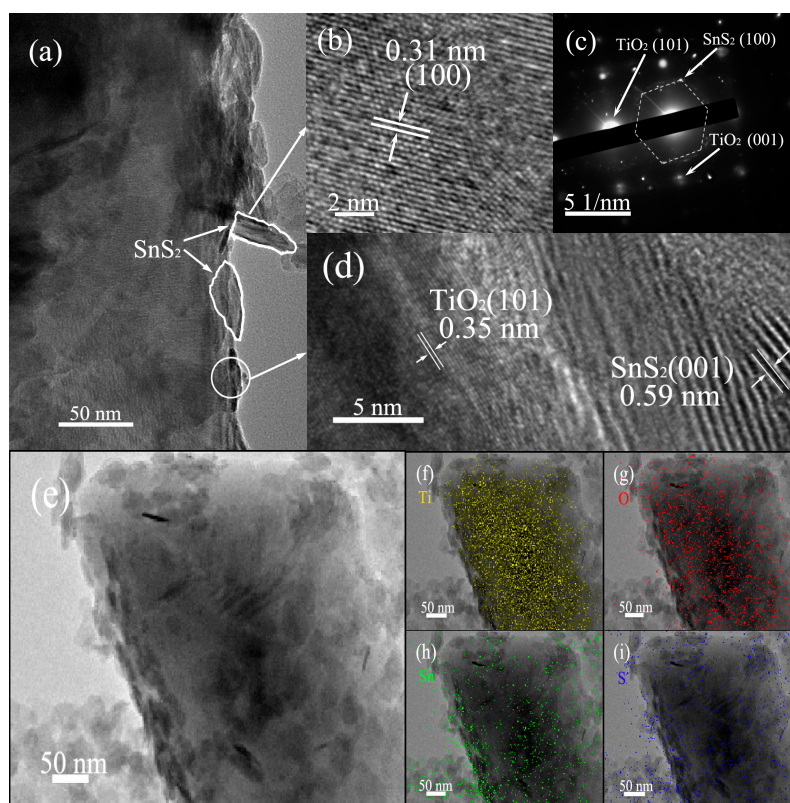**Figure 4.** (**a**) TEM image of a SnS$_2$/TiO$_2$-B nanoplate, (**b**) HRTEM image of SnS$_2$ nanosheets and (**c**) The corresponding SAED pattern, (**d**) HRTEM image at interface region of SnS$_2$/TiO$_2$-B, (**e–i**) The elemental mapping images of SnS$_2$/TiO$_2$-B.

The surface compositions and chemical states of the as-prepared samples have been investigated by XPS. As seen in Figure S3a,b, the full spectra of TiO$_2$-B and SnS$_2$/TiO$_2$-B indicate the presence of elements Ti and O, while SnS$_2$/TiO$_2$-B also displays the existence of S and Sn elements, which are consistent with the above elemental mapping results. Figure 5a shows the comparison of the Ti 2p core-level spectra of samples TiO$_2$-B, TiO$_2$-W, SnS$_2$/TiO$_2$-W and SnS$_2$/TiO$_2$-B. For samples TiO$_2$-B and TiO$_2$-W, two peaks at 458.9 and 464.5 eV are assigned to Ti (IV) 2p$_{3/2}$ and Ti (IV) 2p$_{1/2}$, and another two at 458.2 and 463.9 eV are assigned to Ti (III) 2p$_{3/2}$ and Ti (III) 2p$_{1/2}$, respectively [35,36]. Obviously, the intensities of two Ti (III) 2p peaks decrease significantly for sample TiO$_2$-W, indicating that most of Ti^{3+} ions in TiO$_2$-B are oxidized to Ti^{4+} ions during calcination. Therefore, it is reasonable to use TiO$_2$-W as a control sample without Ti^{3+} defects, and then to explore the role of Ti^{3+} defects in TiO$_2$-B for photocatalytic reduction of CO$_2$. Furthermore, as for SnS$_2$/TiO$_2$-B and SnS$_2$/TiO$_2$-W, the four peaks of Ti 2p all shift to higher binding energy (BE), and the positive shift is even significant for SnS$_2$/TiO$_2$-B, which demonstrates stronger interface interaction between TiO$_2$-B and SnS$_2$. Figure 5b displays the O 1s core-level spectra for SnS$_2$/TiO$_2$-B and SnS$_2$/TiO$_2$-W. The three peaks at the binding energy of 530.4, 531.5 and 532.8 eV are attributed to the Ti−O bond, Ti-OH group and the oxygen vacancy (O$_{VS}$) in the vicinity of Ti^{3+}, respectively [35]. Notably, SnS$_2$/TiO$_2$-B exhibits higher peak intensity corresponding to O$_{VS}$ than that of SnS$_2$/TiO$_2$-W, indicating more oxygen vacancies exist in SnS$_2$/TiO$_2$-B. This is consistent with the above analysis for Ti 2p spectra. In respect of the spectra of Sn 3d shown in Figure 5c, both pure SnS$_2$ and SnS$_2$/TiO$_2$-B show two peaks corresponding to the Sn 3d$_{5/2}$ and Sn 3d$_{3/2}$ of Sn(IV) [27,37,38]. Besides, the S 2p core-level spectra of single SnS$_2$ and SnS$_2$/TiO$_2$-B are given in Figure 5d. It can be seen that the S 2p$_{3/2}$ and S 2p$_{1/2}$ peaks for SnS$_2$ are centered at around 161.3 and 162.5 eV, respectively, which agree with the reference values of S–Sn bond in SnS$_2$ [37]. In contrast, it is observed that binding energies of S 2p$_{3/2}$ and S 2p$_{1/2}$ of SnS$_2$/TiO$_2$-B display the negative shift of 0.3 eV comparing with that of pure SnS$_2$, which might be caused by the interface interaction between

TiO_2-B and SnS_2. Based on the above XPS results, it is clearly demonstrated that TiO_2-B prepared by TiB_2 possesses a large number of the reduced states Ti (III) along with oxygen vacancies, which are maintained well in the composite SnS_2/TiO_2-B. In addition, for SnS_2/TiO_2-B, the strong electronic interaction between TiO_2-B and SnS_2 due to the formation of heterojunction interfaces, could provide an effective channel for the separation and transfer of charge carriers [27,28,39,40].
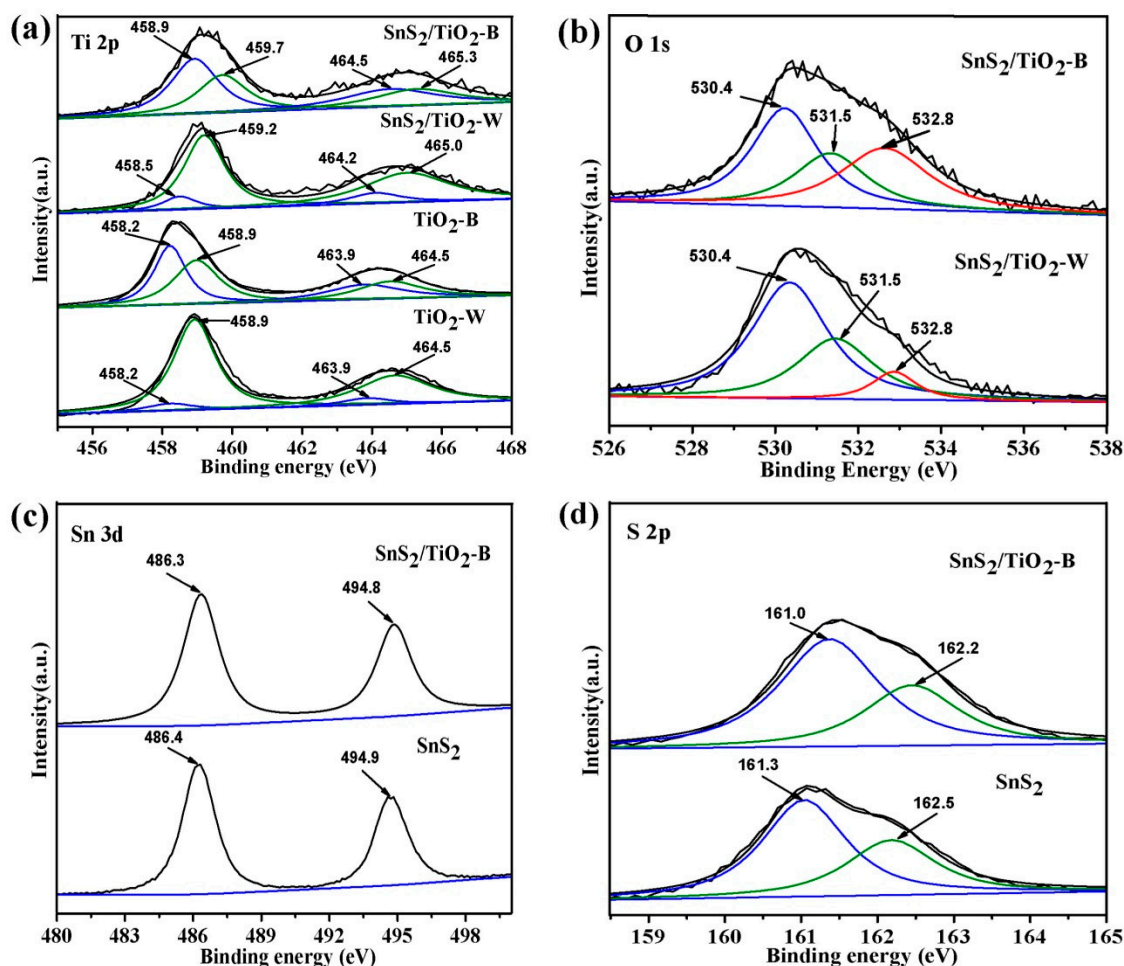

Figure 5. XPS spectra of the as-prepared products: (**a**) Ti 2p core-level spectra, (**b**) O 1s core-level spectra, (**c**) Sn 3d core-level spectra, (**d**) S 2p core-level spectra.

The optical properties of the as-prepared samples have also been investigated. UV−vis absorption spectra are shown in Figure 6a. TiO_2-W exhibits a typical absorption band of the commercial TiO_2 with the absorption edge around 400 nm. In contrast, TiO_2−B shows relatively strong absorption in the UV light range along with strong absorption in visible light region starting from 400 nm, which is in agreement with the photo-absorption profiles of the reported Ti^{3+} defective TiO_2 [41]. As reported, the Ti^{3+} defects form an extra state below the conduction band of TiO_2 with the largest state density at about 0.8 eV, which could extend the photo-response of TiO_2 to visible light range. Moreover, SnS_2, a typical semiconductor with visible light response, shows the light-absorbing ability nearly in the entire UV−vis region [42]. Accordingly, the composite samples with SnS_2, both SnS_2/TiO_2-W and SnS_2/TiO_2-B display the stronger absorption in the visible light region. Worthy of note, SnS_2/TiO_2-B exhibits the most remarkable optical response in the visible light region due to the cooperative contribution to the photo-absorption by SnS_2 and TiO_2-B, which is desirable for achieving high efficient utilization of visible light.
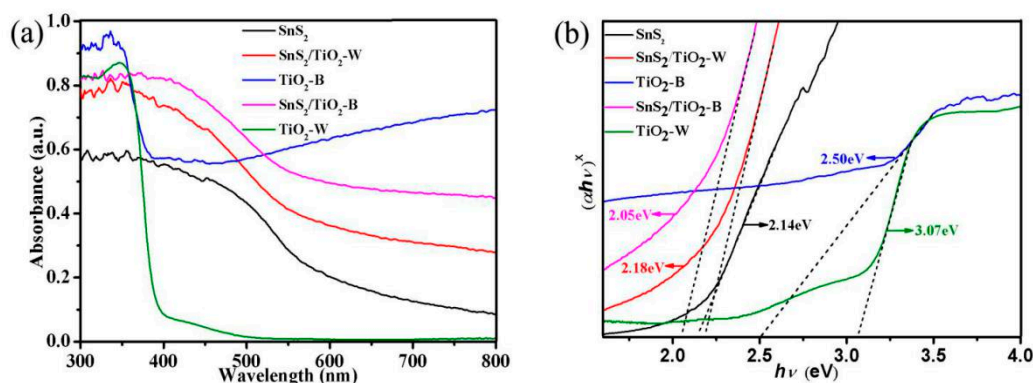
Figure 6. (**a**) UV-Vis absorption spectra of the as-prepared samples, (**b**) The band gaps converted from UV−vis absorption spectra of the as-prepared samples.

The band gaps of the as-prepared samples have been calculated according to the following formula: [43]

$$(\alpha h\nu)^{x} = B\,(h\nu - E_{g})$$ (1)

where α, h, ν, B, and E_{g} are the absorption coefficient, discrete photon energy, a constant and band gap, respectively. Herein, the value of x depends on the characteristics of the transition in a semiconductor: 2 for SnS_2 and 1/2 for TiO_2 based on the definition of direct transition semiconductor (x = 2) and indirect transition semiconductor (x = 1/2), respectively. Taking $h\nu$ as the abscissa axis and $(\alpha h\nu)^{x}$ as the ordinate axis, the corresponding plots are obtained. As shown in Figure 6b, the band gap values of SnS_2 and TiO_2-W are evaluated to be 2.14 and 3.07 eV, respectively, which are consistent with the reported values [27,44]. In comparison with TiO_2-W, TiO_2-B shows much narrower the band gap of 2.50 eV, owing to the presence of Ti^{3+} state lying below the conduction band of TiO_2. What's more, both SnS_2/TiO_2-B and SnS_2/TiO_2-W present even much narrower band gaps of 2.05 and 2.18 eV, respectively. The narrowest band gap of SnS_2/TiO_2-B among these test samples should be ascribed to the synergistic effects resulting from both high-density state of Ti^{3+} and the formation of heterojunction structure between SnS_2/TiO_2-B, which would improve the photocatalytic activity under visible light irradiation.

The Mott−Schottky measurements have been performed to calculate the energy band positions (E_{CB} for conduction band and E_{VB} for valence band) of samples SnS_2/TiO_2-B, SnS_2/TiO_2-W, TiO_2-B, TiO_2-W, and SnS_2. The conduction band potential of a sample can be calculated through the intersection value of the linear part of its MS curve and the abscissa axis [45]. As shown in Figure 7a–e, the slopes of the MS curves for all samples are positive, indicating that they are n-type semiconductors. By fitting the obtained MS curves, the E_{CB} values of SnS_2/TiO_2-B, SnS_2/TiO_2-W, TiO_2-B, TiO_2-W, and SnS_2 are evaluated to be −1.21, −0.78, −0.59, −0.70, −0.90 eV, respectively. Furthermore, the valence band positions of samples can be estimated by the formula ($E_{VB} = E_{g} + E_{CB}$) [46]. Accordingly, the E_{VB} values of SnS_2/TiO_2-B, SnS_2/TiO_2-W, TiO_2-B, TiO_2-W, and SnS_2 are obtained as 0.84, 1.40, 2.00, 2.37, 1.24 eV, respectively. Based on the above results, the band structures of these samples are summarized in Figure 7f. It is indicated that the conduction band potentials of all samples are located above CO_2/CO redox potential, which mean that after the electrons in the valence band of the semiconductor are excited by the photons to the conduction band, the electrons on the conduction band can transition to the CO_2 molecules adsorbed on the surface of the catalyst to carry out the reduction reaction [45,47]. However, from a kinetics point of view, it is, in fact, critical to providing an overpotential, that is, there should be substantial margins over the reduction potential of CO_2. Without an overpotential, even a good catalyst would not ensure a high rate of reaction [38]. Obviously, among these samples, SnS_2/TiO_2-B shows the highest conduction band potential and enough wide band gap spanning the range of the reduction and oxidation potentials, suggesting its strongest reduction ability to convert CO_2 to CO under light irradiation [48].
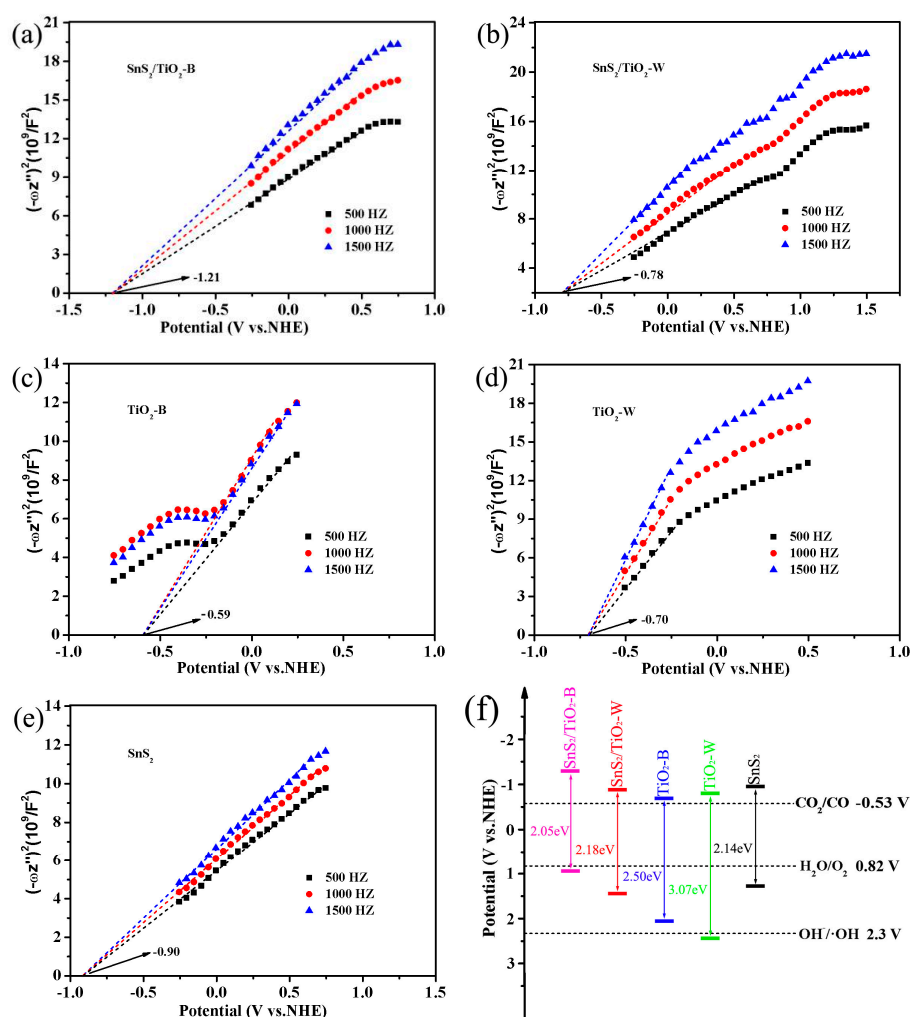
Figure 7. (**a–e**) Mott−Schottky curves of the as-prepared samples, (**f**) Band positions and the band gap energies of the as-prepared samples and the redox potentials of CO_2/CO, H_2O/O_2, and $OH^-/\cdot OH$.

Moreover, the photoluminescence (PL) spectra were applied to evaluate the separation and recombination of the photo-generated charge carriers, which is an important factor for an efficient photocatalyst. Figure 8a depicts the PL spectra of SnS_2/TiO_2-B, SnS_2/TiO_2-W, TiO_2-B, TiO_2-W and SnS_2 with an excitation wavelength $\lambda = 370$ nm. As shown in Figure 8a, TiO_2-B, SnS_2 and TiO_2-W exhibit high PL intensity due to the quick recombination of the electron-hole pairs, which might lead to the lower photocatalytic activity despite having the strong light absorption. According to the literature, Ti^{3+} defects or oxygen vacancies are likely to be the photo-generated electron-hole recombination centers [49–51]. Therefore, it is believed that the high recombination rate for TiO_2-B is caused by the presence of a large amount of Ti^{3+} defects in the bulk TiO_2-B. Generally, the introduction of another semiconductor is an effective approach by constructing the interfacial heterojunction [14]. When their band gap edges match, an electron is preferentially transferred to the semiconductor with the lower CB edge, while a hole moves in the opposite direction to a higher VB level, thereby the recombination rate decreases [38]. Accordingly, upon introducing SnS_2, it is obvious that both SnS_2/TiO_2-B and SnS_2/TiO_2-W show the decreased PL intensity, which confirms that the alignment of the band gap edges between SnS_2 and TiO_2-B or TiO_2-W, thereby suppressing the recombination of electron-hole pairs [29]. Notably, SnS_2/TiO_2-B displays the lowest intensity among samples, which suggests its outstanding ability to separate and transfer the electrons and holes. In addition, the PL peaks of SnS_2/TiO_2-W and SnS_2/TiO_2-B move to the longer wavelength direction between the PL peaks of TiO_2-W, TiO_2-B, and SnS_2, indicating an extension in the absorption range of light through forming a heterojunction [52].

Furthermore, the photocurrent (I_{ph}) responses were also measured to investigate the property of the separation and transfer of the photoinduced charge carriers. As shown in Figure 8b, the photocurrent of SnS_2/TiO_2-B is as high as about 14 and 7 times of those of TiO_2-B and SnS_2 alone, respectively. The higher photocurrent demonstrates that the decoration of SnS_2 on TiO_2-B is able to facilitate the generation of more electron–hole pairs by extending the light absorption range for harvesting more light. In addition, the energetically favorable band alignment between SnS_2 and TiO_2-B is beneficial for promoting efficient interfacial charge transfer.
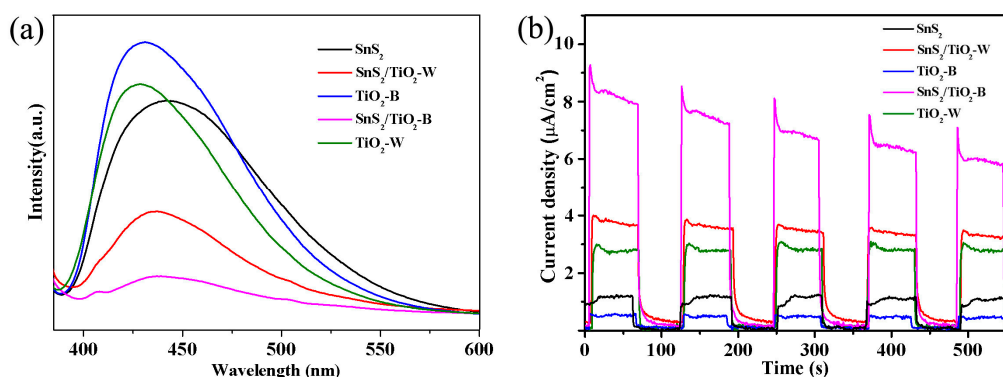

Figure 8. (**a**) The photoluminescence spectrum of the as-prepared samples, (**b**) Photocurrent responses of different samples.

Consequently, the above results demonstrate that combination of SnS_2 and TiO_2-B achieves an optimal band gap, which is not only narrow enough for obtaining strong absorption throughout UV and visible light region but also wide enough for spanning the range of the reduction and oxidation potentials relevant to the photocatalytic reduction of CO_2 and oxidation of H_2O. In addition, the low recombination rate of electron-hole pairs by interface heterojunction and enough overpotential for the reduction of CO_2 to CO are achieved as well. All these advantages could enable it the excellent photocatalytic performance in CO_2 reduction.

2.2. Photocatalytic Activity

The photocatalytic CO_2 reduction reaction was carried out in a 270 mL Pyrex reactor containing 20 mL N, N-dimethylformamide (DMF) and 10 mL ultrapure water. All samples were tested for 4 h under simulated solar light and visible light irradiation, respectively. The gaseous products obtained are analyzed by GC. The results indicate that the main product from CO_2 reduction is CO, while hydrogen is in a negligible amount and no CH_4 or other gases are detected. Figure 9a exhibits the CO production profile with reaction time under simulated solar light irradiation. It can be seen that SnS_2 shows the lowest CO amount during entire reaction period due to the quick recombination of electron-hole pairs as indicated in Figure 8a. While TiO_2-W, SnS_2/TiO_2-W show improved CO production than SnS_2, in agreement with the order of the photocurrent responses shown in Figure 8b. Herein, it is believed that the unique truncated bipyramidal structure of TiO_2 with the co-exposed {101} and {001} facets play an essential role in enhancing reduction of CO_2, possibly through promoting the absorption and activation of CO_2, or the improved separation of electro-hole pairs [12]. By contrast, TiO_2-B shows higher CO production than TiO_2-W, SnS_2/TiO_2-W, and SnS_2, although TiO_2-B displays the lowest photocurrent and highest PL intensity. It is suggested that Ti^{3+} defects play a dominant role in increase CO production. Generally, the efficiency of CO_2 photocatalytic reduction mainly depends on the chemisorption and activation of CO_2, light-harvesting, charge separation, and transfer. It should be noted that the chemisorption and activation of CO_2 is the initial and crucial step in CO_2 photocatalytic reduction. Moreover, it has been reported that oxygen vacancies could enhance the chemisorption of CO_2, and mediate the electron transfer to the adsorbed CO_2 to form the key mediate CO_2^-, thereby promoting the reduction of CO_2 [17]. Upon introducing SnS_2 for improving the

light-harvesting and separation of electron-hole pairs, the photocatalytic properties of SnS_2/TiO_2-B exhibit the highest CO production among samples. For comparison, the CO amount obtained the same reaction was performed for a catalyst of physical mixed TiO_2-B and SnS_2 (SnS_2+TiO_2-B). Obviously, the produced CO amount is much lower than that of SnS_2/TiO_2-B, indicating the important role of the tight interfacial heterojunction in improving the photocatalytic performance. As for the results obtained under visible light irradiation as shown in Figure 9b, the order of the photocatalytic activity does not follow the same trend under simulated solar light conditions. Based on CO production, the catalysts can be classified into three distinctive groups. For SnS_2/TiO_2-W, SnS_2, and TiO_2-W, they hardly produce CO. As for TiO_2-B and (SnS_2+TiO_2-B), they show similar level of CO production, suggesting the main contribution to photocatalytic activity arising from Ti^{3+} defective TiO_2. Remarkably, SnS_2/TiO_2-B presents an exclusively highest CO production than others, which demonstrates its high photocatalytic efficiency solely driven by visible-light. Furthermore, the differences in CO production rates between simulated solar light and visible light irradiation are illustrated for each catalyst, as shown in Figure 9c. It is clear that the catalysts with TiO_2-B component all show significantly higher activity than TiO_2-W samples, revealing that Ti^{3+} defects play the most essential role in the reduction of CO_2. In addition, as shown in Table S1 (Entry 6–9), the control experiments performed under the conditions: under N_2 flow without CO_2 (Entry 6), without light irradiation (Entry 7), only using water without DMF (Entry 8), and only using DMF without water under N_2 flow (Entry 9) were conducted to identify the carbon source of the produced CO. A few amounts of CO and relatively enhanced amounts of H_2 are observed when using water alone, and not-detected amounts of CO is observed in other control experiments. These results demonstrate that the detected CO product is through the photocatalytic reduction of CO_2, not other sources in system. Moreover, the stability test of SnS_2/TiO_2-B was conducted under simulated solar light irradiation and shown in Figure 9d. There is no significant reduction of CO production in the consecutive four cycles, indicating its good stability.
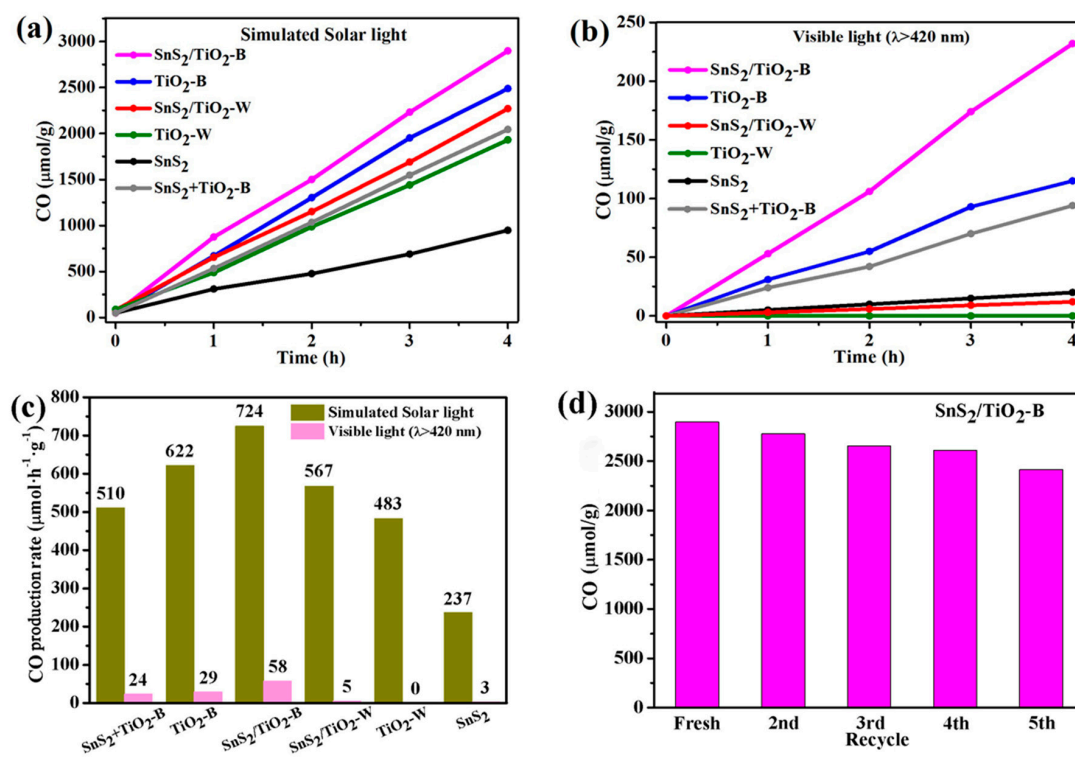

Figure 9. CO production over different photocatalysts (**a**) under simulated solar light and (**b**) visible light (λ > 420 nm) irradiation, (**c**) Comparison of average CO production rates of all samples and (**d**) Stability test of SnS_2/TiO_2-B under simulated solar light irradiation.

2.3. Photocatalytic Mechanism

Based on our results and the reported literature [38,53–56], a plausible mechanism of photocatalytic CO_2 reduction on SnS_2/TiO_2-B is presented in Figure 10. The CB and VB potential TiO_2-B are −0.59 and 2.00 eV, respectively. The Ti^{3+} defects in TiO_2-B cause a sub-band between VB and CB of TiO_2, this sub-band act as a drawing board when photoelectrons are excited to improve the light-harvesting property [53]. Under the radiation of light, the electrons on the VB of TiO_2-B can jump directly to the CB (path (1)), or indirectly transferred to the CB through the Ti^{3+} sub-band (path (2)). However, in TiO_2-W, due to the absence of Ti^{3+} state, the electrons can only directly reach to the CB through (path (1)), which is why TiO_2-W does not absorb visible light (Figure 6a). However, this sub-band also might provide recombination centers of photo-generated electro-hole pairs, thus increasing the recombination rate, evidenced by PL spectrum and photocurrent responses. By forming a heterojunction with SnS_2, due to the higher CB edge at −0.90 eV of SnS_2 and the lower VB edge at 1.24 eV, electron transfer between TiO_2 and SnS_2 may follow two mechanisms (traditional type-II and Z-scheme) [54]. For traditional type-II mechanism, under the radiation of light, SnS_2 and TiO_2 will transfer photo-generated electrons from the higher HOMO level of SnS_2 to the lower CB of TiO_2 and photo-induced holes from the lower VB of TiO_2 to the higher LUMO of SnS_2. In contrast, for Z-scheme shown in Figure 10, the electrons on the VB of TiO_2-B and SnS_2 are excited to the respective CB, along with the formed holes on VB. The electrons on the CB of TiO_2-B tend to jump to the VB of SnS_2 and recombine with holes. Finally, the electrons distributed on the CB of SnS_2 and the holes distributed on the VB of TiO_2-B. Different from the traditional type-II mechanism, the Z-scheme electron transfer mode can make the catalyst exhibit stronger redox ability in the photocatalytic process.
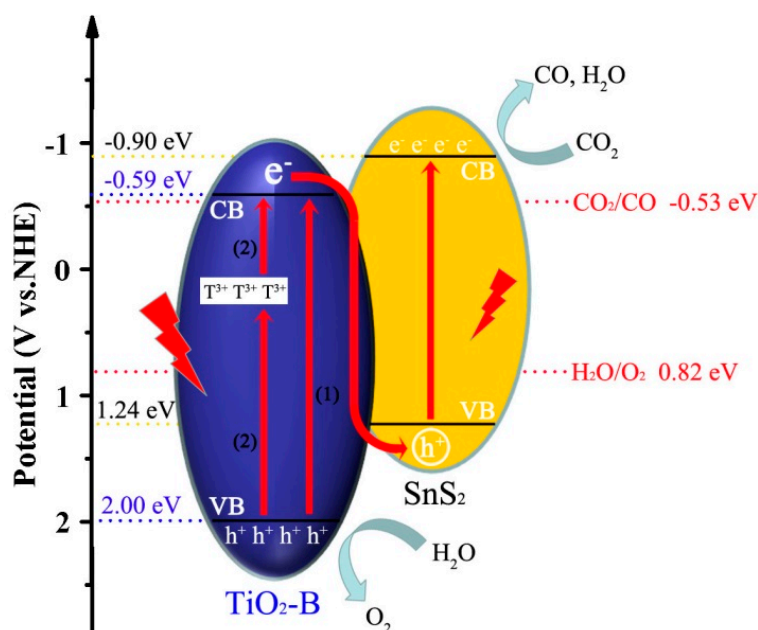

Figure 10. Schematic diagram for interfacial photoexcited electron-hole pairs transfer process.

Herein, it is deluded that the photogenerated charge transfer between TiO_2 and SnS_2 can follow the Z-scheme mode based on the following two points: (1) In the case of the photo-generated electrons following the traditional type-II mode, the electrons transfer to the conduction band of TiO_2-B (−0.59 eV) for the reduction reaction. However, the potential of −0.59 eV could not provide enough overpotential for CO_2 reduction to CO (−0.53 eV). In other words, the reduction ability is too weak to initiate the reduction of CO_2; (2) According to the XPS results in Figure 5, the significant increase in the binding energy of Ti 2p and the contrasting decrease in the binding energy of S 2p could support the transfer of electrons from TiO_2 to SnS_2 due to the formation of a heterojunction interfaces [38]. This Z-scheme

charge transfer mode not only effectively inhibits the recombination of photo-generated electron-hole pairs, but also explains the strong redox capacity of the heterojunction catalyst SnS_2/TiO_2-B. What's more, according to the electron transfer in the Z-scheme mode, CO_2 reduction reaction would occur on SnS_2 surface. As thus, the selective formation of CO while insignificant production of H_2 on SnS_2/TiO_2-B might be reasonably illustrated by the cation–dipole interaction of the lattice Sn^{2+} with DMF leading to a cationic surface, which could prevent the adsorption of H^+, consequently the generation H_2 [55,56].

Overall, the improved photoactivity of SnS_2/TiO_2-B as compared with TiO_2-B, SnS_2 alone and the composite SnS_2/TiO_2-W toward CO_2 reduction can be ascribed to the following factors. On one side, the coupling of SnS_2 with TiO_2-B achieves an optimal band gap size, which is relatively small to absorb light throughout UV and visible light range, and comparably large to span the range of the reduction and oxidation potentials relevant to the photocatalytic reduction of CO_2 and oxidation of H_2O. On another side, the efficient separation and transfer of electrons and holes due to the interface heterojunction and the more reductive conduction band potential toward the reduction of CO_2 to CO are achieved as well.

3. Materials and Methods

3.1. Materials

N,N-dimethylformamide (99.9%, Aladdin), Titanium boride (TiB_2, 99.9% metals basis, 3–5 μm, Aladdin), Poly(sodium 4-styrenesulfonate) (PSS, average Mv ~ 70,000, powder, Aladdin), Hydrofluoric acid aqueous solution (HF, 40%, Shanghai Zhongqin Chemical Reagent Co., Ltd., Shanghai, China), Acetic acid (98.0%, Aladdin, Shanghai, China), Thioacetamide (TAA, 98.0%, Aladdin), Tin(IV) chloride pentahydrate($SnCI_4·5H_2O$, 98.0%, J&K Technology Co., Ltd., Beijing, China). All the reagents were used as received without any further purification. High-purity water (18.25 MΩ·cm) was used in all the experiments.

3.2. Synthesis of Ti^{3+} Defective TiO_2 Nanoplates (TiO_2-B)

In a typical synthesis procedure, 0.5 g of TiB_2 was dispersed in 10 mL of deionized water and was sonicated for 60 min. The resulting suspension was mixed with 8 mL of deionized water and 2 mL of HF aqueous solution under magnetic stirring at 700 rpm. The hydrothermal reaction of the mixture is performed in a 100 mL Teflon-lined autoclave at 180 °C for 12 h. After the reaction, the resulting solid powder was collected by centrifugation and then washed with deionized water three times. Finally, it was dried at 60 °C under vacuum overnight. The obtained dark blue sample was denoted as TiO_2-B. For comparison, TiO_2-W as a control sample without Ti^{3+} defect was prepared by calcining TiO_2-B at 600 °C for 8 h in muffle furnace.

3.3. Synthesis of SnS_2/TiO_2-B Photocatalyst

A total of 0.15 g of as-prepared TiO_2-B was added to 20 mL aqueous solution of Poly (sodium 4-styrenesulfonate) of 0.3%, and the mixture was sonicated ultrasonication for 20 min. The solid was recovered by centrifugation and washed three times with deionized water, then dispersed in 20 mL deionized water. Next, 0.086 g $SnCI_4·5H_2O$, 0.092 g thioacetamide (TAA) and 1 mL acetic acid were added under stirring. Five minutes later, the resulting suspension was transferred into a 100 mL Teflon-lined autoclave and heated at 160 °C for 12 h. After the reaction, the resulting solid powders were collected by centrifugation and washed with deionized water three times and finally dried at 60 °C under vacuum overnight. The resultant sample was denoted as SnS_2/TiO_2-B. Using TiO_2-W as a substrate, the control sample SnS_2/TiO_2-W was obtained. In the absence of the TiO_2, we prepared the sample SnS_2 nanosheets.

3.4. Characterization

The X-ray diffraction (XRD, Rigaku D/MAX-2500 diffractometer, Tokyo, Japan) with Cu Kα radiation was recorded to determine the crystal structure of the samples. The scanning electron microscopy (SEM, Hitachi S-4800, Tokyo, Japan) was performed to analyze the morphology and structure of materials. High-resolution TEM was carried out on a Tecnai G2 F-20 transmission electron microscope. A UV-vis spectrophotometer (Instant Spec BWS003 spectrometers, Shanghai, China) was used to obtain the optical absorbance spectra of the samples. The surface composition and chemical states were analyzed by X-ray photoelectron spectroscopy (XPS) on a PHI 1600 (PerkinElmer, Waltham, MA, USA) analyzer with X-ray excitation provided by an Al Kα X-ray source, and all the XPS spectra were calibrated by C1s binding energy which is 284.6 eV. Steady-state photoluminescence (PL) spectra were measured using a Horiba JobinYvon Fluorolog 3–21 with excitation at 370 nm. Photoelectrochemical measurements were recorded with an Autolab 302N Electrochemical System. An Ag/AgCl and a Pt plate were used as the reference electrode and the counter electrode, respectively. A glassy carbon electrode (GCE, 1.0 cm $\times$ 1.0 cm) coated with catalyst was used as a working electrode. Na_2SO_4 (0.5 M) was used as electrolyte solution. Photocurrent curves of the samples were collected as switching the light source every 60 s at a potential of 0.2 V.

3.5. Photocatalytic CO_2 Reduction Measurements

The photocatalytic CO_2 reduction reaction was carried out in a 270 mL Pyrex reactor under ultraviolet-visible irradiation (300 W Xe lamp), visible light was obtained with a 400 nm long-pass filter. In brief, 30 mg catalyst was dispersed into 30 mL reaction suspension containing 20 mL N, N-dimethylformamide and 10 mL ultrapure water. Prior to the illumination, high purity CO_2 was bubbled through the reactor for 30 min, allowing the reactor to be filled with CO_2 (1 bar) while venting the air. The reaction temperature was maintained at 25 °C with a cooling water circulator. The gases were analyzed using gas chromatography equipped with a thermal conductive detector (TCD) and a TDX-01 packed molecular sieves column.

4. Conclusions

In summary, we have successfully synthesized dark blue TiO_2 nanoplates containing a large amount of Ti^{3+} defects. This method is simple, safe and energy-efficient compared to the post-treatment for doping Ti^{3+} defect into TiO_2. After characterization, we found that Ti^{3+} defects help to increase the absorption of visible light. However, a large number of Ti^{3+} defects also inhibit the separation of photo-generated electron-hole pairs, which is not conducive to the photocatalytic reaction. Upon introducing SnS_2, the heterojunction catalyst SnS_2/TiO_2-B not only possesses the strong light absorption from UV to visible light region, the lowest photo-generated charge recombination rate but also achieves a more negative conduction band potential than the reduction potential of CO_2 to CO, and thereby exhibits the significantly enhanced selectivity and yield of CO in photocatalytic CO_2 reduction. Notably, SnS_2/TiO_2-B produces CO at a rate of 58 μmol·h^{-1}·g^{-1} under visible light irradiation, which is 2 and 19 times greater than those of alone TiO_2-B and SnS_2, respectively. Finally, a plausible photocatalytic mechanism on SnS_2/TiO_2-B was proposed that the electron transfer between TiO_2 and SnS_2 follows the Z-scheme mechanism. Our results present an effective way to gain highly efficient TiO_2 based photocatalysts for CO_2 reduction by combining different modification methods of TiO_2 and make full use of the synergistic effects.

Author Contributions: Conceptualization, H.W.; Data curation, A.H., M.L., S.Z. and H.W.; Formal analysis, A.H.; Funding acquisition, H.W., Q.G., X.Z.; Investigation, A.H.; Methodology, A.H., M.L. and S.Z.; Project

Conflicts of Interest: The authors declare no conflict of interest.

References

1. Wang, L.; Duan, S.; Jin, P.; She, H.; Huang, J.; Lei, Z.; Zhang, T.; Wang, Q. Anchored Cu(II) tetra(4-carboxylphenyl)porphyrin to P25 (TiO_2) for efficient photocatalytic ability in CO_2 reduction. *Appl. Catal. B* **2018**, *239*, 599–608. [CrossRef]

2. Tan, L.; Ong, W.; Chai, S.; Mohamed, A.R. Visible-light-activated oxygen-rich TiO_2 as next generation photocatalyst: Importance of annealing temperature on the photoactivity toward reduction of carbon dioxide. *Chem. Eng. J.* **2016**, *283*, 1254–1263. [CrossRef]

3. Tu, W.; Zhou, Y.; Zou, Z. Photocatalytic conversion of CO_2 into renewable hydrocarbon fuels: State-of-the-art accomplishment, challenges, and prospects. *Adv. Mater.* **2014**, *26*, 4607–4626. [CrossRef]

4. Guo, X.L.; Kuang, M.; Li, F.; Liu, X.Y.; Zhang, Y.X.; Dong, F.; Losic, D. Engineering of three dimensional (3-D) diatom@TiO_2@MnO_2 composites with enhanced supercapacitor performance. *Electrochim. Acta* **2016**, *190*, 159–167. [CrossRef]

5. Zhao, Z.; Zhang, W.; Lv, X.; Sun, Y.; Dong, F.; Zhang, Y. Noble metal-free Bi nanoparticles supported on TiO_2 with plasmon-enhanced visible light photocatalytic air purification. *Environ. Sci. Nano* **2016**, *3*, 1306–1317. [CrossRef]

6. Wang, Q.; Lian, J.; Bai, Y.; Hui, J.; Zhong, J.; Li, J.; An, N.; Yu, J.; Wang, F. Photocatalytic activity of hydrogen production from water over TiO_2 with different crystal structures. *Mater. Sci. Semicond. Process.* **2015**, *40*, 418–423. [CrossRef]

7. Zhang, Q.; Gao, T.; Andino, J.M.; Li, Y. Copper and iodine co-modified TiO_2 nanoparticles for improved activity of CO_2 photoreduction with water vapor. *Appl. Catal. B* **2012**, *123*, 257–264. [CrossRef]

8. Pan, J.; Liu, G.; Lu, G.Q.M.; Cheng, H. On the true photoreactivity order of {001}, {010}, and {101} facets of anatase TiO_2 crystals. *Angew. Chem. Int. Ed.* **2011**, *50*, 2133–2137. [CrossRef]

9. Wang, G.; Wang, H.; Ling, Y.; Tang, Y.; Yang, X.; Fitzmorris, R.C.; Wang, C.; Zhang, J.Z.; Li, Y. Hydrogen-treated TiO_2 nanowire arrays for photo-electrochemical water splitting. *Nano Lett.* **2011**, *11*, 3026–3033. [CrossRef]

10. Akhavan, O.; Ghaderi, E. Photocatalytic reduction of graphene oxide nanosheets on TiO_2 thin film for photoinactivation of bacteria in solar light irradiation. *J. Phys. Chem. C* **2009**, *113*, 20214–20220. [CrossRef]

11. Ye, L.; Mao, J.; Peng, T.; Zan, L.; Zhang, Y. Opposite photocatalytic activity orders of low-index facets of anatase TiO_2 for liquid phase dye degradation and gaseous phase CO_2 photoreduction. *Phys. Chem. Chem. Phys.* **2014**, *16*, 15675–15680. [CrossRef] [PubMed]

12. Yu, J.; Low, J.; Xiao, W.; Zhou, P.; Jaroniec, M. Enhanced photocatalytic CO_2 reduction activity of anatase TiO_2 by co-exposed {001} and {101} facets. *J. Am. Chem. Soc.* **2014**, *136*, 8839–8842. [CrossRef]

13. Wang, P.; Jia, C.; Li, J.; Yang, P. Ti^{3+}-doped TiO_2 (B)/anatase spheres prepared using thioglycolic acid towards super photocatalysis performance. *J. Alloy. Compd.* **2019**, *780*, 660–670. [CrossRef]

14. Liu, X.; Du, G.; Li, M. True photoreactivity origin of Ti^{3+}-Doped anatase TiO_2 crystals with respectively dominated exposed {001}, {101}, and {100} facets. *ACS Omega* **2019**, *4*, 14902–14912. [CrossRef]

15. Umer, M.; Tahir, M.; Azam, M.U.; Tahir, B.; Musaab, M. Self-doped Ti^{3+} mediated TiO_2/In_2O_3/SWCNTs heterojunction composite under acidic/basic heat medium for boosting visible light induced H_2 evolution. *Int. J. Hydrog. Energy* **2019**, *44*, 13466–13479. [CrossRef]

16. Fang, W.; Khrouz, L.; Zhou, Y.; Shen, B.; Dong, C.; Xing, M.; Mishra, S.; Daniele, S.; Zhang, J. Reduced {001}-TiO_{2-x} photocatalysts: Noble-metal-free CO_2 photoreduction for selective CH_4 evolution. *Phys. Chem. Chem. Phys.* **2017**, *19*, 13875–13881. [CrossRef] [PubMed]

17. Pipornpong, W.; Wanbayor, R.; Ruangpornvisuti, V. Adsorption CO_2 on the perfect and oxygen vacancy defect surfaces of anatase TiO_2 and its photocatalytic mechanism of conversion to CO. *Appl. Surf. Sci.* **2011**, *257*, 10322–10328. [CrossRef]

18. Janbandhu, S.Y.; Joshi, A.; Munishwar, S.R.; Gedam, R.S. CdS/TiO$_2$ heterojunction in glass matrix: Synthesis, characterization, and application as an improved photocatalyst. *Appl. Surf. Sci.* **2019**, *497*, 143758–143769. [CrossRef]

19. Zhang, X.; Gao, Y.; Nengzi, L.; Li, B.; Gou, J.; Cheng, X. Synthesis of SnS/TiO$_2$ nano-tube arrays photoelectrode and its high photoelectrocatalytic performance for elimination of 2,4,6-trichlorophenol. *Sep. Purif. Technol.* **2019**, *228*, 115742–115750. [CrossRef]

20. Pan, X.; Yang, M.; Fu, X.; Zhang, N.; Xu, Y. Defective TiO$_2$ with oxygen vacancies: Synthesis, properties and photocatalytic applications. *Nanoscale* **2013**, *5*, 3601–3614. [CrossRef]

21. Liu, L.; Zhao, C.; Miller, J.T.; Li, Y. Mechanistic study of CO$_2$ photoreduction with H$_2$O on Cu/TiO$_2$ nanocomposites by in situ X-ray absorption and infrared spectroscopies. *J. Phys. Chem. C* **2016**, *121*, 490–499. [CrossRef]

22. Liu, G.; Yang, H.G.; Wang, X.; Cheng, L.; Lu, H.; Wang, L.; Lu, G.Q.M.; Cheng, H. Enhanced photoactivity of oxygen-deficient anatase TiO$_2$ sheets with dominant {001} facets. *J. Phys. Chem. C* **2009**, *113*, 21784–21788. [CrossRef]

23. Zhao, J.; Xing, W.; Li, Y.; Lu, K. Solvothermal synthesis and visible light absorption of anatase TiO$_2$. *Mater. Lett.* **2015**, *145*, 332–335. [CrossRef]

24. Huo, Y.; Yang, Y.; Dai, K.; Zhang, J. Construction of 2D/2D porous graphitic C$_3$N$_4$/SnS$_2$ composite as a direct Z-scheme system for efficient visible photocatalytic activity. *Appl. Surf. Sci.* **2019**, *481*, 1260–1269. [CrossRef]

25. Song, Y.; Gu, J.; Xia, K.; Yi, J.; Chen, H.; She, X.; Chen, Z.; Ding, C.; Li, H.; Xu, H. Construction of 2D SnS$_2$/g-C$_3$N$_4$ Z-scheme composite with superior visible-light photocatalytic performance. *Appl. Surf. Sci.* **2019**, *467*, 56–64. [CrossRef]

26. Su, Y.; Wang, C.; Zhang, Y.; Yang, Z.; Dionysiou, D.D. Design and preparation of SnO$_2$/SnS$_2$/conjugated polyvinyl chloride derivative ternary composite with enhanced visible-light photocatalytic activity. *Mater. Res. Bull.* **2019**, *118*, 110524. [CrossRef]

27. Zhang, Z.; Shao, C.; Li, X.; Sun, Y.; Zhang, M.; Mu, J.; Zhang, P.; Guo, Z.; Liu, Y. Hierarchical assembly of ultrathin hexagonal SnS$_2$ nanosheets onto electrospun TiO$_2$ nanofibers: Enhanced photocatalytic activity based on photoinduced interfacial charge transfer. *Nanoscale* **2013**, *5*, 606–618. [CrossRef]

28. Zhang, Y.C.; Li, J.; Xu, H.Y. One-step in situ solvothermal synthesis of SnS$_2$/TiO$_2$ nanocomposites with high performance in visible light-driven photocatalytic reduction of aqueous Cr (VI). *Appl. Catal. B* **2012**, *123*, 18–26. [CrossRef]

29. She, H.; Zhou, H.; Li, L.; Zhao, Z.; Jiang, M.; Huang, J.; Wang, L.; Wang, Q. Construction of a two-dimensional composite derived from TiO$_2$ and SnS$_2$ for enhanced photocatalytic reduction of CO$_2$ into CH$_4$. *ACS Sustain. Chem. Eng.* **2018**, *7*, 650–659. [CrossRef]

30. Yang, H.G.; Sun, C.H.; Qiao, S.Z.; Zou, J.; Liu, G.; Smith, S.C.; Cheng, H.M.; Lu, G.Q. Anatase TiO$_2$ single crystals with a large percentage of reactive facets. *Nature* **2008**, *453*, 638–641. [CrossRef]

31. Liu, G.; Yang, H.G.; Sun, C.; Cheng, L.; Wang, L.; Lu, G.Q.M.; Cheng, H. Titania polymorphs derived from crystalline titanium diboride. *CrystEngComm* **2009**, *11*, 2677–2682. [CrossRef]

32. Chiesa, M.; Livraghi, S.; Giamello, E.; Albanese, E.; Pacchioni, G. Ferromagnetic interactions in highly stable, partially reduced TiO$_2$; the S = 2 State in anatase. *Angew. Chem. Int. Ed.* **2017**, *56*, 2604–2607. [CrossRef] [PubMed]

33. Zhang, Z.; Huang, J.; Zhang, M.; Yuan, Q.; Dong, B. Ultrathin hexagonal SnS$_2$ nanosheets coupled with g-C$_3$N$_4$ nanosheets as 2D/2D heterojunction photocatalysts toward high photocatalytic activity. *Appl. Catal. B* **2015**, *163*, 298–305. [CrossRef]

34. Gordon, T.R.; Cargnello, M.; Paik, T.; Mangolini, F.; Weber, R.T.; Fornasiero, P.; Murray, C.B. Nonaqueous synthesis of TiO$_2$ nanocrystals using TiF$_4$ to engineer morphology, oxygen vacancy concentration, and photocatalytic activity. *J. Am. Chem. Soc.* **2012**, *134*, 6751–6761. [CrossRef] [PubMed]

35. Liu, C.; Wu, P.; Wu, J.; Hou, J.; Bai, H.; Liu, Z. Effective protect of oxygen vacancies in carbon layer coated black TiO$_2$−x/CNNS hetero-junction photocatalyst. *Chem. Eng. J.* **2019**, *359*, 58–68. [CrossRef]

36. Shen, L.; Xing, Z.; Zou, J.; Li, Z.; Wu, X.; Zhang, Y.; Zhu, Q.; Yang, S.; Zhou, W. Black TiO$_2$ nanobelts/g-C$_3$N$_4$ nanosheets laminated heterojunctions with efficient visible-light-driven photocatalytic performance. *Sci. Rep.* **2017**, *7*, 41978–41988. [CrossRef] [PubMed]

37. Zhang, Y.C.; Li, J.; Zhang, M.; Dionysiou, D.D. Size-tunable hydrothermal synthesis of SnS_2 nanocrystals with high performance in visible light-driven photocatalytic reduction of aqueous Cr (VI). *Environ. Sci. Technol.* **2011**, *45*, 9324–9331. [CrossRef]

38. Zhang, S.; Li, M.; Zhao, J.; Wang, H.; Zhu, X.; Han, J.; Liu, X. Plasmonic AuPd-based Mott-Schottky photocatalyst for synergistically enhanced hydrogen evolution from formic acid and aldehyde. *Appl. Catal. B* **2019**, *252*, 24–32. [CrossRef]

39. Zhang, Z.; Shao, C.; Li, X.; Wang, C.; Zhang, M.; Liu, Y. Electrospun nanofibers of p-type NiO/n-type ZnO heterojunctions with enhanced photocatalytic activity. *ACS Appl. Mater. Interfaces* **2010**, *2*, 2915–2923. [CrossRef]

40. Zheng, Y.; Zheng, L.; Zhan, Y.; Lin, X.; Zheng, Q.; Wei, K. Ag/ZnO heterostructure nanocrystals: Synthesis, characterization, and photocatalysis. *Inorg. Chem.* **2007**, *46*, 6980–6986. [CrossRef]

41. Chen, X.; Liu, L.; Huang, F. Black titanium dioxide (TiO_2) nanomaterials. *Chem. Soc. Rev.* **2015**, *44*, 1861–1885. [CrossRef] [PubMed]

42. Sun, L.; Zhao, Z.; Li, S.; Su, Y.; Huang, L.; Shao, N.; Liu, F.; Bu, Y.; Zhang, H.; Zhang, Z. Role of SnS_2 in 2D–2D SnS_2/TiO_2 nanosheet heterojunctions for photocatalytic hydrogen evolution. *ACS Appl. Nano Mater.* **2019**, *2*, 2144–2151. [CrossRef]

43. Butler, M.A. Photoelectrolysis and physical properties of the semiconducting electrode WO_2. *J. Appl. Phys.* **1977**, *48*, 1914–1920. [CrossRef]

44. Pian, X.; Lin, B.; Chen, Y.; Kuang, J.; Zhang, K.; Fu, L. Pillared nanocomposite TiO_2/Bi-Doped hexaniobate with visible-light photocatalytic activity. *J. Phys. Chem. C* **2011**, *115*, 6531–6539. [CrossRef]

45. Liang, H.; Acharjya, A.; Anito, D.A.; Vogl, S.; Wang, T.; Thomas, A.; Han, B. Rhenium-metalated polypyridine-based porous polycarbazoles for visible-light CO_2 photoreduction. *ACS Catal.* **2019**, *9*, 3959–3968. [CrossRef]

46. Lu, J.; Li, D.; Chai, Y.; Li, L.; Li, M.; Zhang, Y.; Liang, J. Rational design and preparation of nanoheterostructures based on zinc titanate for solar-driven photocatalytic conversion of CO_2 to valuable fuels. *Appl. Catal. B* **2019**, *256*, 117800. [CrossRef]

47. Habisreutinger, S.N.; Schmidt-Mende, L.; Stolarczyk, J.K. Photocatalytic reduction of CO_2 on TiO_2 and other semiconductors. *Angew. Chem. Int. Ed.* **2013**, *52*, 7372–7408. [CrossRef]

48. Xing, M.; Zhou, Y.; Dong, C.; Cai, L.; Zeng, L.; Shen, B.; Pan, L.; Dong, C.; Chai, Y.; Zhang, J.; et al. Modulation of the reduction potential of TiO_{2-x} by fluorination for efficient and selective CH_4 generation from CO_2 photoreduction. *Nano Lett.* **2018**, *18*, 3384–3390. [CrossRef]

49. Wang, J.; Tafen, D.N.; Lewis, J.P.; Hong, Z.; Manivannan, A.; Zhi, M.; Li, M.; Wu, N. Origin of photocatalytic activity of nitrogen-doped TiO_2 nanobelts. *J. Am. Chem. Soc.* **2009**, *131*, 12290–12297. [CrossRef]

50. Pan, X.; Zhang, N.; Fu, X.; Xu, Y. Selective oxidation of benzyl alcohol over TiO_2 nanosheets with exposed {001} facets: Catalyst deactivation and regeneration. *Appl. Catal. A* **2013**, *453*, 181–187. [CrossRef]

51. Xie, T.; Lin, J. Origin of photocatalytic deactivation of TiO_2 film coated on ceramic substrate. *J. Phys. Chem. C* **2007**, *111*, 9968–9974. [CrossRef]

52. Qin, J.; Wang, S.; Ren, H.; Hou, Y.; Wang, X. Photocatalytic reduction of CO_2 by graphitic carbon nitride polymers derived from urea and barbituric acid. *Appl. Catal. B* **2015**, *179*, 1–8. [CrossRef]

53. Li, J.; Zhang, M.; Guan, Z.; Li, Q.; He, C.; Yang, J. Synergistic effect of surface and bulk single-electron-trapped oxygen vacancy of TiO_2 in the photocatalytic reduction of CO_2. *Appl. Catal. B* **2017**, *206*, 300–307. [CrossRef]

54. Kong, L.; Zhang, X.; Wang, C.; Xu, J.; Du, X.; Li, L. Ti^{3+} defect mediated g-C_3N_4/TiO_2 Z-scheme system for enhanced photocatalytic redox performance. *Appl. Surf. Sci.* **2018**, *448*, 288–296. [CrossRef]

55. Fujiwar, H.; Hosokawa, H.; Murakoshi, K.; Wada, Y.; Yanagida, S. Effect of surface structures on photocatalytic CO_2 reduction using quantized CdS nanocrystallites1. *J. Phys. Chem. B* **1997**, *101*, 8270–8278. [CrossRef]

56. Liu, B.; Torimoto, T.; Yoneyama, H. Photocatalytic reduction of CO_2 using surface-modified CdS photocatalysts in organic solvents. *J. Photochem. Photobiol. A* **1998**, *113*, 93–97. [CrossRef]